AIAA-2004-1111

FUNDAMENTAL INVESTIGATION OF SUPERSONIC NOZZLE FLOW SEPARATION

Dimitri Papamoschou *
Andreas Zill †
University of California, Irvine, California 92697-3975

We present preliminary experimental results on separation of supersonic flow inside a convergent-divergent (CD) nozzle. The study is motivated by the occurrence of mixing enhancement outside CD nozzles operated at low pressure ratio. A novel apparatus allows investigation of many nozzle geometries with large optical access and measurement of wall and centerline pressures. The nozzle area ratio ranged from 1.0 to 1.5 and the pressure ratio ranged from 1.2 to 1.8. At the low end of these ranges, the shock is nearly straight. As the area ratio and pressure ratio increase, the shock acquires two lambda feet. Towards the high end of the ranges, one lambda foot is consistently larger than the other and flow separation occurs asymmetrically. Downstream of the shock, flow accelerates to supersonic speed and then recompresses. The shock is unsteady, however there is no evidence of resonant tones. The separation shear layer on the side of the large lambda foot exhibits intense instability that grows into huge eddies downstream of the nozzle exit. It appears that asymmetric flow separation is a key ingredient in the mixing enhancement mechanism.

Nomenclature

a	=	speed of sound
A	=	cross sectional area
F	=	thrust
H	=	nozzle height
$\dot{m}$	=	mass flow rate
M	=	Mach number
p	=	static pressure
p_0	=	total pressure
U	=	velocity
x	=	axial distance from nozzle throat
θ	=	wall angle

Subscripts

a	=	ambient
d	=	design point
e	=	exit
s	=	shock
t	=	throat

*Professor, Associate Fellow AIAA
†Graduate student, Member AIAA

Introduction

Separation of supersonic flow in a convergent-divergent nozzle is a basic fluid-dynamics phenomenon that occurs in a variety of aerospace applications. When a supersonic nozzle is operating at pressure ratios well below its design point, a shock forms inside the nozzle and flow downstream of the shock separates from the nozzle walls. Even though this flow is very basic, it remains poorly understood. This is illustrated by the large discrepancy between predictions of quasi-one-dimensional inviscid theory and the actual behavior of the flow, as will be shown in this paper. Even though separation is typically viewed as an undesirable occurrence, it may have some interesting applications in the area of fluid mixing. Specifically, past work at U.C. Irvine has shown that flow exiting a severely-overexpanded nozzle exhibits a strong instability that enhances mixing of the flow itself and of an adjacent flow. Figure 1 presents an example. The resulting method of Mixing Enhancement via Secondary Parallel Injection (MESPI) has been proven in a variety of circular and rectangular nozzles [1, 2, 3]. The physical mechanisms behind this method remain obscure, hence the need to study the fundamental fluid me-

chanics of supersonic nozzle flow separation.

Supersonic nozzle flow separation occurs in convergent-divergent nozzles subjected to pressure ratios much below their design value, resulting in shock formation inside the nozzle. In the one-dimensional, inviscid treatment of Fig. 2a, the shock is normal and the flow past the shock stays attached to the wall, thus compresses subsonically to the ambient static pressure. In reality, flow detaches and forms a separation region near the wall, as depicted in Fig. 2b. For moderate nozzle area ratios a lambda shock is often observed. Flow downstream of the shock is non-uniform and its structure is very complex.

There is a large volume of literature dealing with separation in rocket nozzles, which have large expansion ratios. A paramount issue is prediction of separation location, specifically the ratio p_s/p_a (pressure just ahead of separation over ambient pressure). A review of the older literature, and correlation of experimental results in a large variety of nozzles, is given by Morrisette & Goldberg [4]. Their primary conclusion is that zero-pressure-gradient separation predictors, like the method of Reshotko & Tucker [5], give reasonable predictions for nozzles with turbulent separation and large divergence angles. The ratio p_s/p_a is a declining function of the shock Mach number M_s and, as a rule of thumb, is roughly 0.5 for $M_s \approx 2$ and 0.3 for $M_s \approx 4$. Nozzles with laminar separation exhibited higher separation pressure ratios. Separation in nozzles with low local wall angles, such as low-divergence conical nozzles and contoured nozzles, deviated from the above predictions. The close proximity of the wall to the separation shear layer has been cited as a possible reason for the discrepancy.

Computational studies of two-dimensional overexpanded nozzles by Wilmoth & Leavitt [6] and by Hamed & Voyatzis [7, 8] assessed the accuracy of turbulence models for predicting the flow field and thrust performance. The works agree on the basic structure of the separation shock, which consists of the incident shock, Mach stem (normal shock), and reflected shock. Thrust predictions were in good agreement with experiments, except at pressure ratios associated with separated flow. A combined experimental and computational work by Hunter [9] offers one of the most comprehensive treatments of this flow. His experimental results on a two-dimensional nozzle with $A_e/A_t = 1.8$ showed two distinct separation regimes: three-dimensional separation with partial reattachment for nozzle pressure ratio NPR$\leq$ 1.8 and fully-detached two-dimensional separation for NPR $\geq$ 2.0. Hunter claims that this transition was not the result of markedly different onset conditions or stronger shock-boundary layer interaction, but instead came about trough the natural tendency of an overexpanded nozzle flow to detach and reach a more efficient thermodynamic balance. As a result, the thrust of the separated case is much higher that that given by inviscid analysis. Notable in Hunter's experiments and simulations was the much higher nozzle pressure ratio required to situate the shock at a given area ratio compared to the inviscid prediction. For example, to place the normal shock just outside the nozzle exit a nozzle pressure ratio NPR=3.4 was required, versus NPR=1.8 predicted in the inviscid case.

Generic methods for boundary-layer separation cannot capture the entirety of events inside a nozzle. Recently, a theoretical model proposed by Romine [11] fills this gap. For shocks with moderate Mach numbers (less than 2.25), Romine postulates that the jet flow emerging from the shock is above ambient pressure and adjusts to the ambient pressure via a gradual underexpansion. The magnitude of the underexpansion is equal to that of the overall overexpansion. It is important to note that this argument applies in the vicinity of the *centerline* of the nozzle, where the shock is normal, and not on the walls. On the walls, Romine postulates that flow adjusts to the ambient pressure almost immediately past the shock. The underexpansion is evident in the computational Mach number contours of Hunter [9], although he did not mention it explicitly.

An interesting phenomenon related to supersonic nozzle flow separation is that of "aeroacoustic resonance," studied by Zaman et al. [10]. It occurs often, but not always, in convergent-divergent nozzles operated at low pressure ratios, and is characterized by strong acoustic tones and their harmonics. The work by Zaman et al. connected the tone generation to the unsteadiness of the shock system and showed that the frequencies scale with the distance from the shock foot to the nozzle exit. Tripping the nozzle's internal boundary layer suppresses the tones. Aeroacoustic resonance was an early suspect mechanism for the MESPI phenomenon. However, it was largely ruled out because mixing enhancement persisted with or without resonant tones [12].

Experiment

It was desired to study nozzle separation in an apparatus that affords flexibility in wall geometry and optical diagnostic access. Accordingly, a novel facility, shown in Fig. 3, was constructed. The upper and lower walls of the nozzle consist of flexible plates that can assume a variety of shapes. Nozzle shaping is achieved by actuators, mounted at the end of each plate, that control the transverse force and moment applied at the end of each plate. This mechanism allows variations of the nozzle area ratio, nozzle contour, and maximum wall angle. Investigation of "half-nozzles" is also possible by deflecting only one of the plates. The nominal test section dimensions are 22.9 mm in height, 63.5 mm in width, and 117 mm in length from throat to exit. The sidewalls of the nozzle incorporate large optical windows for visualization of the entire internal flow, from the subsonic converging section to the nozzle exit. The apparatus is connected to a system that delivers pressure-regulated air and air mixed with either helium or argon. The use of variable-density gas is primarily a means of controlling the Reynolds number and specific heat ratio. The facility is designed for a maximum nozzle pressure of 3.5, which allows investigation of the entire sequence of internal events (from subsonic flow, to flow with shocks, to shock-free flow) in nozzles with exit-to-throat area ratios up to 1.60.

In the study reported here, the nozzle walls were diverged symmetrically by applying force only (no moment) on the actuators. Consequently, each wall assumed the shape of a cantilevered beam with point force applied to its end, and the nozzle was "trumpet-shaped" with the wall angle increasing monotonically from throat to exit. Pure air was supplied at nozzle pressure ratio (NPR=p_{0_1}/p_a) up to about 1.8. The maximum level of NPR was dictated by the mass flow limitations of the facility.

The upper and lower wall each incorporate 24 static pressure ports that are equally-spaced in the axial direction and are arranged along the midwidth of the nozzle. Each row of ports starts upstream of the nozzle throat, at area ratio $A/A_t = 1.14$, and ends at the nozzle exit. The diameter of each port on the surface of the nozzle is 0.8 mm.

Diagnostic tools for this study consisted of spark schlieren photography of the internal and external flow; wall pressure measurement; nozzle centerline pressure measurement; and recording of the sound in the vicinity of the nozzle exit.

The Schlieren system employed a 20-nanosecond spark as a light source (Xenon, Model N787), lenses with 150-mm diameter and 1-m focal length for collimating the beam, and a charged coupled device (CCD) camera for acquiring the images (Sony, Cybershot). The spatial resolution of the images was 2560×1712 pixels.

The nozzle wall ports were scanned by a mechanical pressure multiplexer (Scanivalve, Model SSS-48), which consists of a pneumatic selector switch connected to a single pressure transducer (Setra, Model 280). The use of a single transducer simplified calibration and thus increases the reliability of the pressure measurement. For the experiments reported here, the scan rate was 3 ports per second.

The static pressure along the centerline of the nozzle and jet plume was measured by a 0.5-mm static port drilled into a 2.4-mm-diameter strainless-steel tube that was translated axially along the nozzle. See Fig. 4 for the centerline pressure measurement system. The upstream end of the tube was capped and the downstream end was connected to a pressure transducer (Setra, Model 280). The upstream end of the tube was supported by the honeycomb flow straightener, thus did not introduce any appreciable disturbance into the flow. The downstream end was attached to streamlined strut placed far from the nozzle exit. The strut and tube assembly was translated by a motorized linear actuation stage mounted on the nozzle structure but placed completely outside the jet flow. The orifice in the steel tube traveled from 24 mm upstream of the nozzle throat to 20 mm downstream of the nozzle exit. The tube occupied 0.3% of the nominal nozzle cross sectional area of the nozzle, and the flow deflection it caused (due to boundary layer formation on the tube) was extremely small. Thus, the presence of the tube in the test section did not change the flow phenomena inside and outside the nozzle. A similar method was used circa 1903 by Stodola [13] to measure the centerline pressure distribution in an axisymmetric Laval nozzle.

To record the noise emitted by the internal flow phenomena and the external jet flow, a condenser microphone (Bruel & Kjaer, Model 4133) was situated at a distance of 300 mm from the nozzle exit and angle of 45° relative to the jet axis. The microphone recordings were processed into sound spectra corrected for microphone response and atmospheric absorption.

Results

Schlieren Photography

Spark schlieren photography captured the instantaneous features of the shock system and the ensuing turbulent flow separation. We present in Figs. 5 and 6 the sequence of shock formation as NPR increases for $A_e/A_t = 1.2$ and 1.5, respectively. For both area ratios, a well-defined shock appears at NPR around 1.2. For the lower area ratio, the shock is symmetric and nearly straight for low to moderate NPRs. For NPR > 1.4, the shock acquires symmetric "lambda feet" near the walls. Each lambda foot is characterized by the incident shock, reflected shock, and the triple point where the incident and reflected shocks merge into the Mach stem. A slipstream (entropy layer) originates at each triple point. For $A_e/A_t = 1.5$, lambda feet appear at NPR=1.3 and become progressively larger with increasing NPR. Except at very low value of NPR, the shock structure is asymmetric and exhibits a large lambda foot on one side and a small one on the other side. For $A_e/A_t \geq 1.4$ and NPR > 1.3, we never observed symmetric formation of the shock. The shock asymmetry could be specific to the shape of the nozzles used here.

During the duration of a given test, which lasted up to 15 seconds, the asymmetry of the shock did not change, i.e., the lambda feet did not flip. We verified this by flashing the spark gap at high frequency and recording the images on a video camera (in essence, taking a movie of the flow but with time-uncorrelated frames). However, when we stopped and restarted the flow, at exactly the same pressure ratio and nozzle geometry, the shock asymmetry could flip. In other words, the shock chooses its orientation at the start-up of the run and retains the same orientation throughout the run. The asymmetry of the flow could be the manifestation of a "Coanda effect" whereby a jet surrounded by or adjacent to a solid surface attaches to the surface.

The separation shear layer downstream of the large lambda foot grows rapidly and displays very strong instability. In contrast, the shear layer emerging from the small lambda foot is stable. Figure 7 shows details of the shock structure and separated flow. Very large eddies, sometimes occupying more than half the test section height, are seen to emerge downstream of the large lamda foot. For large area ratios, the shock system is unsteady in the axial direction but not exceedingly so. The axial travel distance was on the order of half the local test section height and the variation in shock Mach number was around 4%.

Another very important feature of the flow is the succession of weak normal shocks ("aftershocks") past main shock. This phenomenon occurred in all our visualizations but is particularly well captured in the photographs of Fig. 7. The presence of shocks downstream of the main part of the separation shock indicates that flow accelerates to supersonic speed, recompresses, reaccelerates, etc. This means that, immediately downstream of the Mach stem, there is no pressure recovery. Instead, there is an underexpansion. Close examination of Fig. 7 shows expansion fans emanating from the intersection of the reflected shocks with the separation shear layers. Evidently, the reflected shock of the lambda foot is of the "weak" type, i.e., flow downstream of the shock is supersonic. The interaction of the shock with the shear layer is very similar to the boundary layer-shock interaction studied by Liepmann [16] in transonic flows over airfoils.

The presence of shocks spanning the entire jet of the separated flow (not confined to the supersonic region past each lambda foot) indicates that flow downstream of the main shock accelerates to speeds that have locally supersonic values. This must be accomplished by the slipstream forming sonic throat and then diverging. The presence of multiple shocks suggests that, further downstream, the slipstream creates additional sonic throats until it decelerates to subsonic Mach numbers. Thus, it appears that a "wavy" slipstream is created that supports alternation of subsonic and supersonic flow. The flow images suggest that the expansion waves emanating from the intersection of the reflected shock with the shear layer are transmitted through the slipstream, which means that the slipstream is supersonic at the position where it is intercepted by the expansion waves. The nearly-straight shape of the aftershocks further suggests that the entire jet acquires a nearly-uniform velocity a short distance past the Mach stem. The above observations are summarized in the sketch of Fig. 8.

A large number of pictures was processed to obtain the shock position versus area ratio and pressure ratio. Shock position A_s/A_t is defined as the area ratio corresponding to the axial position of the Mach stem (normal part) of the shock. Figure 9 plots the shock position versus NPR for four nozzle area ratios. Notable is the substantial discrepancy

between the actual shock position and the position predicted by one-dimensional inviscid theory. The discrepancy worsens with increasing area ratio. The shock sits at an area ratio much smaller than that predicted by the theory. The physical reason is the the underexpansion, noted above, that forms immediately downstream of the normal shock. The underexpansion creates a "back pressure" much higher than the theory predicts, causing the shock to sit at a smaller than expected area ratio. As mentioned in the Introduction, the discrepancy with theory was evident by a few data points collected by previous investigations. We believe, however, that this is the first systematic study of shock location versus area ratio and pressure ratio. Future studies will include the effect of wall angle. Deviation of the shock location data from the best fit curves in Fig. 9 is an indication of shock unsteadiness. Unsteadiness increases with area ratio.

Wall Pressure

Static pressure distributions along the upper wall of the nozzle are plotted in Fig. 10 for various nozzle pressure ratios and three area ratios. Since the nozzle is symmetric, there are no noticeable differences between the upper and lower wall pressure distributions except at large area ratios and large nozzle pressure ratios. The pressure distributions have the "classic" shape of expansion, shock jump, and recovery. The major difference from the theoretical case is that, for a give pressure ratio, the shock Mach number, and therefore the pressure jump, are much smaller.

As mentioned in the previous section, for large A_e/A_t and NPR$>$ 1.4, the shock structure is asymmetric. This creates a small change in the pressure distributions on the upper and lower nozzle surfaces. Figure 11 compares the upper and lower wall pressure distributions for $Ae/A_t = 1.5$ and NPR=1.61. There is a distinct difference in the pressure recovery past the shock. On the side of the large lambda foot, pressure recovers linearly with distance. This type of recovery is similar to the "strong-shock" recovery in diffusers measured by Sajben at al. [14] and predicted numerically by Xiao et al. [15]. On the side of the small lambda foot, the pressure shows a faster initial rise followed by a gradual recovery to ambient value. The asymmetric recovery creates a small sideward force generated on the nozzle, which we calculate to be around 1-2% of the nozzle thrust.

It is important to note that the wall pressure past the separation shock does not adjust to the ambient pressure immediately. While an immediate pressure adjustment occurs in large-area-ratio nozzles, in nozzles with small to moderate pressure ratio the adjustment is gradual. This means that Romine's theory [11], which assumes immediate recovery, is not applicable here unless the shock sits at the nozzle exit.

Centerline Pressure

Figure 12 plots the centerline pressure distribution, measured with the translating tube of Fig. 4, for various area ratios and nozzle pressure ratios. The trends are similar to those for the wall pressure, except that the "recovery" past the shock has a different shape. For NPR$>$ 1.5, pressure past the shock shows a flat region, or a slight dip, followed by a gradual rise to the ambient value. A direct comparison between wall and centerline pressures is shown in Fig. 13. The pressure rise on the centerline is sharper than that on the walls. The pressure dip that follows is qualitatively consistent with the conjecture of Fig. 8. However, the quantitative behavior in the vicinity of the shock was surprising at first.

In contrast to the complex shock structure near the wall, the shock near the nozzle centerline is a clean normal shock. We thus expect the pressure rise across the shock to follow the normal-shock relation

$$\frac{p_2}{p_1} = 1 + \frac{2\gamma}{\gamma+1}(M_1^2 - 1) \qquad (1)$$

where M_1 is the flow Mach number immediately upstream of the shock and is related to the local static pressure p_1 via

$$\frac{p_1}{p_{0_1}} = \left(1 + \frac{\gamma-1}{2}M_1^2\right)^{\frac{-\gamma}{\gamma-1}} \qquad (2)$$

Combining Eqs. 1 and 2 we arrive at a relation of p_2 versus solely p_1,

$$\frac{p_2}{p_{0_1}} = \frac{4\gamma}{\gamma^2-1}\left(\frac{p_1}{p_{0_1}}\right)^{\frac{1}{\gamma}} - \frac{(\gamma+1)^2}{\gamma^2-1}\frac{p_1}{p_{0_1}} \qquad (3)$$

which is plotted in Fig. 14. It is evident from the plots of Fig. 12 that the measured pressure rise across the shock does not satisfy Eq. 3. To clarify this point, we plot in Fig. 15a the centerline pressure distribution for $A_e/A_t = 1.5$ and NPR=1.61. Just

before the shock, we have p_1/p_{0_1}=0.30. The peak pressure of the shock is $p/p_{0_1} = 0.55$, much less than the normal-shock solution $p_2/p_{0_1} = 0.67$. One could argue that, since the shock is unsteady, the steady normal shock relations may not hold. Since we do not know the details of the shock motion (it is not harmonic, as will be shown later), we cannot fully answer this point. On the other hand, we can make the simple argument that a velocity u_s of the shock relative to a stationary observer should increase the mean pressure ratio: the shock Mach number becomes $M_s = M_1 + u_s/a_1$ and the pressure ratio depends on the square of the shock Mach number. Moreover, we know from the visualizations that flow past the shock undergoes a substantial expansion that is not shown in the measurements. So the behavior of the centerline pressure distribution cannot be explained by a possible effect of unsteadiness on the normal shock relations.

It will now be shown that the shape of the centerline pressure distribution is likely the result of smoothing due to the shock motion. The centerline probe does not measure the true pressure distribution but a filtered distribution, which can be expressed as the convolution of the true pressure $p(x)$ with a response function $r(x)$

$$p_{\text{meas}}(x) \;=\; \int p(\xi)\; r(x-\xi) d\xi \qquad (4)$$

For response function we assume a Gaussian kernel

$$r(x) \;=\; \frac{1}{b\sqrt{\pi}} e^{-(x/b)^2} \qquad (5)$$

Evaluation of Eq. 4 was done using Fourier transforms. The pressure distribution of Fig. 15a was reshaped into a hypothetical distribution, shown in Fig. 15b, having a nearly-discontinuous pressure jump that satisfies the normal shock relations. The shock of this hypothetical curve was placed in the middle of the shock rise of the measured pressure distribution. The pressure before the shock was calculated by extrapolating linearly the measured data upstream of the shock to the shock location, resulting in $p_1/p_{0_1} = 0.27$. The pressure jump is followed by a rapid expansion that brings the pressure down to the level of the small plateau that forms past the shock in the measured data.

Figure 15b shows the result of smoothing of the hypothetical pressure distribution with a Gaussian kernel having full-width $2b = 13$ mm. The smoothed curve and the actual curve of Fig. 15a practically coincide. The Gaussian full-width is about one half of the test section height, which agrees with our visual observation of shock motion. Of course, the hypothetical curve of Fig. 15b is not unique and this exercise is neither a rigorous nor a perfect reconstruction of the true pressure distribution. Using sophisticated deconvolution methods one may be able to recover the true pressure distribution without any assumptions, but the numerical challenges are significant. What we have shown here is that the measured pressure distributions is consistent with Gaussian smoothing of a pressure distribution that satisfies the normal shock relations.

Importantly, the hypothetical curve of Fig. 15b clarifies the flow process in the vicinity of the nozzle centerline for the conditions examined in this experiment. Instead of a monotonic adjustment to the ambient pressure, we have expansion followed by compression. We already observed in the flow visualizations that the expansion results from the reflection of the reflected shock of the lambda foot from the shear layer of the separation zone. As long as the reflected shock is of the "weak" type (i.e., the outflow is supersonic), an expansion is inevitable. Flow past the the Mach stem needs to adjust to this lower pressure, therefore it also accelerates to supersonic speed, as illustrated by Fig. 8. The expansion brings the pressure to a level below ambient, thus a compression is needed for matching the ambient pressure. The last statement applies for the range of conditions examined in this study. It is possible that, for very strong shocks, the adjustment to ambient pressure involves only an expansion.

The normal-shock relation of Eq. 3, plotted of Fig. 14, merits further discussion. It is straightforward to show that the maximum of p_2/p_{0_1} occurs at

$$\frac{p_1}{p_{0_1}} \;=\; \left(\frac{\gamma+1}{2}\right)^{\frac{2\gamma}{1-\gamma}} \;=\; 0.279 \;\text{ for } \gamma = 1.4$$

and has the value

$$\frac{p_2}{p_{0_1}} \;=\; 2\left(\frac{\gamma+1}{2}\right)^{\frac{\gamma+1}{1-\gamma}} \;=\; 0.670 \;\text{ for } \gamma = 1.4$$

The value of p_1/p_{0_1} for which the maximum occurs is the square of the critical pressure ratio $[(\gamma+1)/2]^{(1-\gamma)/\gamma}$ =0.528 for $\gamma = 1.4$. The corresponding Mach number is $M_1 = 1.483$ and the corresponding area ratio is $A_1/A_t = 1.165$. The right termination of the curve of Fig. 15 corresponds to sonic flow for which both pressure ratios equal the critical value of 0.528. For $0.528 < p_2/p_{0_1} < 0.670$ and $A_1/A_t > 1.165$, two solutions exist for p_1/p_{0_1}. Gen-

erally p_2 is not an independent variable, so the ramifications of Fig. 14 on shock instability are not clear. However, if the relation between p_2 and the ambient pressure p_a were known, then Fig. 15 offers guidance as to the possibility of shock instability caused by the double-valuedness of the solution. For example, if $p_2 = p_a$, then $p_2/p_{0_1} = p_a/p_{0_1} = 1/\text{NPR}$ and double-valuedness occurs for $1.492 < \text{NPR} < 1.893$.

Thrust

Given that one of the intended applications of the mixing enhancement phenomenon is on aeroengines, it is important to assess the thrust loss caused by flow separation inside a convergent-divergent nozzle. From the above results it is clear that one-dimensional theory would be very inadequate for thrust prediction. This experiment has generated results – the wall pressure distributions – that allow an estimate of thrust loss. This estimate will not include shear stresses; however, their impact is much smaller than the impact of the pressure distribution created by the shock.

The procedure for calculating thrust is explained in Fig. 16. For simplicity, and without loss of generality, we consider a "half nozzle." The ideal thrust is created by the "design" nozzle for given NPR. Specifically, the design nozzle it is a nozzle with the same NPR and mass flow rate as the actual nozzle, that produces a shock-free flow with pressure-matched exhaust. For subcritical nozzle pressure ratios (NPR < 1.893 for $\gamma = 1.4$), the shape of the design nozzle is convergent. With respect to the full nozzle shown in Fig. 16a, the design nozzle comprises the portion of the nozzle upstream of the design point "d" where $p = p_a$. The resulting nozzle, shown in Fig. 16b, has the same NPR and same mass flow rate as the actual nozzle.

The thrust of a nozzle equals the integral of the axial components of the forces acting on the internal and external walls of the nozzle and supply reservoir. Here we deal only with pressure forces. At static conditions, the external pressure is ambient, p_a. A portion of the internal pressure distribution p (from a short distance upstream of the nozzle throat to the nozzle exit) is known from our measurements. Letting s denote the coordinate along the surface of the nozzle and θ the local angle of the surface, the thrust of the actual nozzle is

$$F = \int_o^e (p - p_a) \sin\theta ds \qquad (6)$$

The thrust integral can be divided into two parts, the contribution upstream of the design point and the contribution downstream of the design point:

$$F = \int_o^d (p - p_a) \sin\theta ds + \int_d^e (p - p_a) \sin\theta ds \qquad (7)$$

The first integral represents the ideal thrust, which equals the momentum flux of the perfectly expanded flow:

$$F_i = \int_o^d (p - p_a) \sin\theta ds = \dot{m} U_d \qquad (8)$$

where $\dot{m}$ is the mass flow rate and U_d is the design (perfectly-expanded) velocity. Therefore the actual thrust is

$$F = \dot{m} U_d + \int_d^e (p - p_a) \sin\theta ds \qquad (9)$$

and the thrust coefficient is

$$\frac{F}{F_i} = 1 + \frac{1}{\dot{m} U_d} \int_d^e (p - p_a) \sin\theta ds \qquad (10)$$

The mass flow rate is based on the sonic conditions in the actual nozzle,

$$\dot{m} = A_t \gamma \frac{p_{0_1}}{a_0} \left(\frac{\gamma + 1}{2} \right)^{\frac{\gamma+1}{1-\gamma}} \qquad (11)$$

where $a_0 = \sqrt{\gamma R T_0}$ is the reservoir speed of sound. The fully-expanded velocity is given by the relation

$$U_d = a_0 \sqrt{\frac{2}{\gamma - 1} \left(1 - \text{NPR}^{(1-\gamma)/\gamma} \right)} \qquad (12)$$

Integration of the pressure started at the point "d", where $p = p_a$, and ended at the nozzle exit. For NPR$<$1.35, point "d" was located upstream of the first static pressure port, therefore it could not be resolved. For this reason, the thrust calculation was performed for NPR > 1.35.

Figure 17 shows the thrust coefficient versus NPR for various nozzle area ratios. For $A_e/A_t < 1.5$, the thrust coefficient drops then rises with increasing NPR. For $A_e/A_t = 1.5$ the thrust coefficient is seen to rise monotonically with NPR, although it is possible that a minimum occurs at NPR < 1.35. As expected, the thrust coefficient drops with increasing area ratio, a consequence of stronger shocks and higher total pressure loss. The overall trends and values are consistent with those of past works that measured nozzle thrust directly [9, 6]. It is important to note that in many envisioned applications,

such as military engines, the thrust allocated to mixing enhancement would be on the order of 10-20% of the total engine thrust [3]. Thus, a loss of 7% in the thrust of the secondary flow used for mixing enhancement translates to a thrust loss on the order of 1% for the entire engine.

Noise

Figure 18 shows sound spectra for the lowest and higher NPRs and for various nozzle area ratios. The spectra look like typical jet noise spectra. As expected, flow at the higher NPR is louder because of the larger exit velocity and mass flow rate. There is no marked change in the shape of the spectra as the area ratio varies. Also, there is no presence of any tones. In contrast, past work by Zaman et al. [10], measured strong resonance tones in small nozzles operated at low pressure ratios. The phenomenon of aeroacoustic resonance depends on the state of the boundary layers at separation, and possibly on the nozzle cross-sectional shape. In our experiments, flow visualization shows that the boundary layers prior to separation were turbulent. In the experiments of Zaman et al., it is likely that the boundary layers were laminar. Importantly, resonance was suppressed when the internal nozzle boundary layer was tripped. Collectively, this information suggests that aeroacoustic resonance does not occur when the boundary layer is turbulent. Given the complexity of this phenomenon, however, it is premature to proclaim any firm conclusions.

Still, the shock wave is unstable, as revealed by flow vizualization and the smoothing exercise of Fig. 15. The microphone measurements suggest that the motion of the shock is not coherent and therefore not the result of an acoustic feedback loop. Instead, the shock motion could be caused by the large instability of the shear layers downstream of the shock. In other words, the shear layer instability is driving the shock motion and not vice-versa.

Mixing

The Flow Visualization section already described the development of very large eddies inside the test section when the area ratio is large, i.e., $A_e/A_t \geq 1.4$. Now we look at the related fluid phenomena outside the test section. Recall that for $A_e/A_t \geq 1.4$ and NPR$>$ 1.5 flow separation always occurred asymmetrically. Figure 19 shows a selection of spark schlieren photographs for $A_e/A_t = 1.0$, 1.4 amd 1.5. Because the refractive index gradients outside the nozzle become weak, the images were enhanced using the linear-ramp algorithm of [18]. For $A_e/A_t = 1.0$, the shear layers of the external jet grow at a relatively slow rate. For the larger area ratios, the shear layer on the side of the large separation zone is very unstable and forms huge eddies. The shear layer on the side of the small separation zone grows at a mixing rate similar to that of a normal jet.

The cause of the formation of the huge eddies is not yet clear. As we have seen previously, the separation jet is subjected to significant pressure gradients, first favorable and then adverse. Although the wall and centerline pressures at the nozzle exit are seen to balance in the mean sense, instantaneously there may be significant inbalances giving rise to substantial flow deflections. This issue will be addressed in future experiments using time-resolved pressure measurements.

Concluding Remarks

Supersonic nozzle flow separation is an extremely complex phenomenon. Our preliminary study, motivated by the phenomenon of mixing enhancement, has shed some light on the salient flow phenomena but many unknowns remain. The range of flow conditions was $1.0 < A_e/A_t < 1.5$ and $1.2 <$ NPR $<$ 1.8. We summarize our findings as follows:

1. For $A_e/A_t > 1.2$ and NPR > 1.4, the separation shock has a well-defined lambda shape. For large values of A_e/A_t and NPR, one lambda foot is always larger than the other, i.e., separation occurs asymmetrically. The asymmetry does not flip during a given test run, but can change side from run to run.

2. Flow downstream of the Mach stem expands to near-sonic speed and exhibits an alternation of subsonic and supersonic flow. The expansion is due to the reflection of the trailing shock of the lambda foot from the separation pressure boundary. Eventually, the flow compresses to subsonic speed and matches the ambient pressure.

3. The shock forms at an area ratio much smaller than that predicted by one-dimensional inviscid theory. The theory assumes that, past

the shock, flow is attached and compresses to the ambient pressure. In reality, flow is detached and initially expands. As a result, the "back pressure" felt by the shock is substantially larger than the theoretical prediction. This drives the shock towards the throat.

4. For large NPR and A_e/A_t, the shock is unsteady and the range of its axial motion is approximately one half of the local test section height. The shock motion smooths out the centerline pressure distribution measured by a static pressure probe, thereby obliterating critical features of the true pressure distribution.

5. The separation shear layer on the side of the large lambda foot exhibits intense instability that grows into huge eddies downstream of the nozzle exit. The shear layer on the side of the small lambda foot grows normally. Thus, the MESPI phenomenon seems to be connected with asymmetric flow separation.

6. There is no evidence of resonant tones. The apparent lack of acoustic feedback indicates that the shock motion is caused by the shear layer instability and not vice-versa.

One important factor not included in our study is the effect of wall angle on separation. Our apparatus gives us the flexibility to vary the wall angle while maintaining a constant area ratio. Also, there is clear need for time-resolved measurements of the static pressure along the walls and on the centerline of the nozzle. We hope to address these issues in the near future.

Acknowledgments

The support by the National Science Foundation (Grant No. CTS-0072964) and by NASA Glenn Research Center (Grant NAG-3-2345 monitored by Dr. Khairul B. Zaman) is gratefully acknowledged.

References

[1] Papamoschou, D., "Mixing Enhancement Using Axial Flow," AIAA-2000-0093.

[2] Murakami, E. and Papamoschou, D., "Experiments on Mixing Enhancement in Dual-Stream Jets," AIAA-2001-0668.

[3] Papamoschou, D., Dixon, T.D., and Nishi, K., "Mean Flow of Multi-Stream Rectangular Jets under Normal and Mixing-Enhancement Conditions," AIAA-2004-0919.

[4] Morrisette, E.L., and Goldberg, T.J., "Turbulent Flow Separation Criteria for Overexpanded Supersonic Nozzles," NASA TP 1207, Aug. 1978.

[5] Reshotko, E., and Tucker, M., "Effect of a Discontinuity on Turbulent Boundary Layer Thickness Parameters with Application to Shock-Induced Separation," NACA TN-3454, 1955.

[6] Wilmoth, R.G., and Leavitt, L.D., "Navier Stokes Predictions of Multifunction Nozzle Flows," *Society of Automotive Engineers Transactions*, Vol. 96, Sec.6, Paper 871753, 1987, pp. 6.865-6.879.

[7] Hamed, A., and Vogiatzis, C., "Overexpanded Two-Dimensional Convergent-Divergent Nozzle Flow Simulations, Assessment of Turbulence Models," *Journal of Propulsion and Power*, Vol. 13, No. 3, 1997, pp. 444-445.

[8] Hamed, A., and Vogiatzis, C., "Overexpanded Two-Dimensional Convergent-Divergent Nozzle Performance, Effects of Three-Dimensional Flow Interactions," *Journal of Propulsion and Power*, Vol. 14, No. 2, 1998, pp. 234-240.

[9] Hunter, C.A., "Experimental, Theoretical and Computational Investigation of Separated Nozzle Flows," AIAA-98-3107.

[10] Zaman, K.B.M.Q., Dahl, M.D., Bencic, T.J., and Loh, C.Y., "Investigation of a Transonic Resonance with Convergent-Divergent Nozzles," *Journal of Fluid Mechanics*," Vol. 263, 2002, pp. 313-343.

[11] Romine, G.L., "Nozzle Flow Separation," *AIAA Journal*, Vol. 36, No.9, 1998, pp. 1618-1625.

[12] Zaman, K.B.M.Q, and Papamoschou, D., "Study of Mixing Enhancement Observed with a Co-Annular Nozzle Configuration, " AIAA-2000-0094.

[13] Anderson, J.D.,"Modern Compresible Flow," 2nd Ed., McGraw Hill, New York, 1990, pp. 179-181.

[14] Sajben, M., Bogar, T.J., and Kroutil, J.C., "Characteristic Frequencies of Transonic Diffuser Flow Oscillations," *AIAA Journal*, Vol. 21, No.9, 1983, pp. 1232-1240.

[15] Xiao, Q., Tsai, H.M., and Liu, F., "Computation of Transonic Diffuser Flows by a Legged $k-\omega$ Turbulence Model," *AIAA Journal of Propulsion and Power*, Vol. 19, No. 3, pp. 473-483.

[16] Liepmann, H.W., "The Interaction Between Boundary Layer and Shock Waves in Transonic Flow," *Journal of the Aeronautical Sciences*," Vol. 13, No. 12, 1946, pp. 623-637.

[17] Miller, E.H., and Migdal, D., "Separation and Stability Studies of a Convergent-Divergent Nozzle," *AIAA Journal of Aircraft*, Vol. 7, No.2, 1970, pp. 159-163.

[18] Papamoschou, D., "Mach Wave Elimination in Supersonic Jets," *AIAA Journal*, Vol. 35, No.10, 1997, pp. 1604-1611

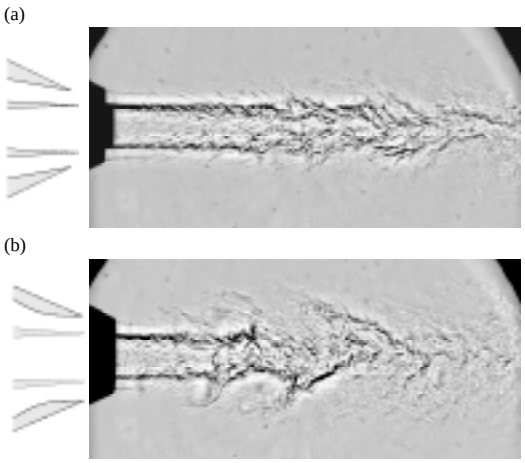

Fig.1 Primary jet flow at Mach 0.9 surrounded by an annular secondary flow at nozzle pressure ratio NPR=1.7. (a) secondary nozzle is convergent; (b) secondary nozzle is convergent-divergent. The strong instability in case (b) is one of the motivations for studying the phenomenon of supersonic nozzle flow separation.

Table 1 Flow conditions

A_e/A_t	θ_e (deg)	NPR_{min}	NPR_{max}
1.00	0.00	1.41	1.77
1.20	1.56	1.30	1.59
1.30	2.33	1.29	1.61
1.40	3.17	1.26	1.77
1.50	3.89	1.27	1.61

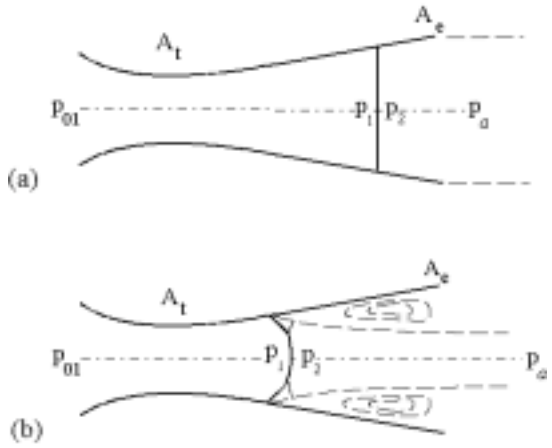

Fig.2 Sketch of shock structure and fluid phenomena for overexpanded nozzle. (a) Inviscid case; (b) viscous (separated) case.

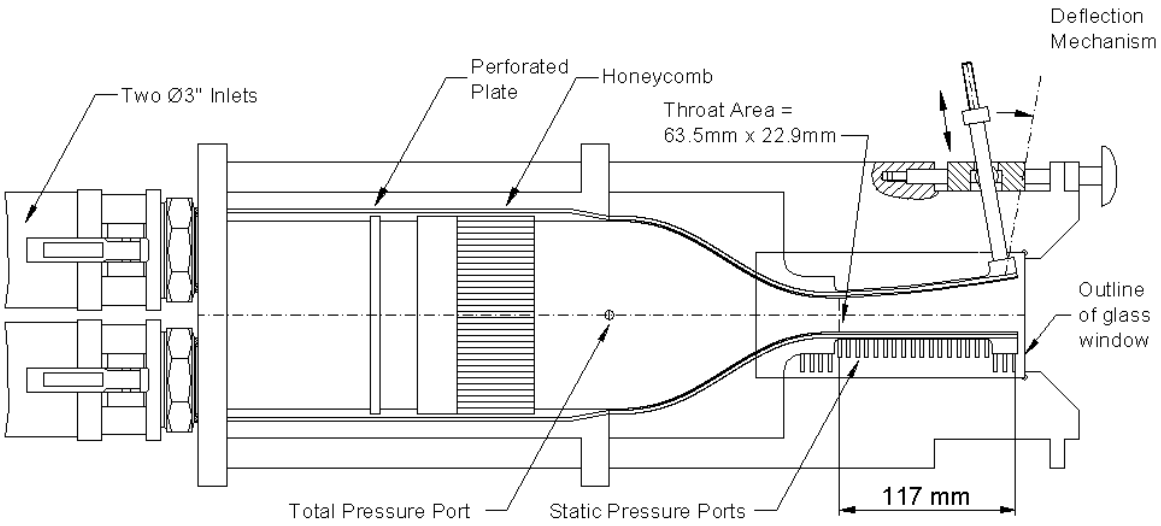

Fig.3 Schematic of variable nozzle apparatus.

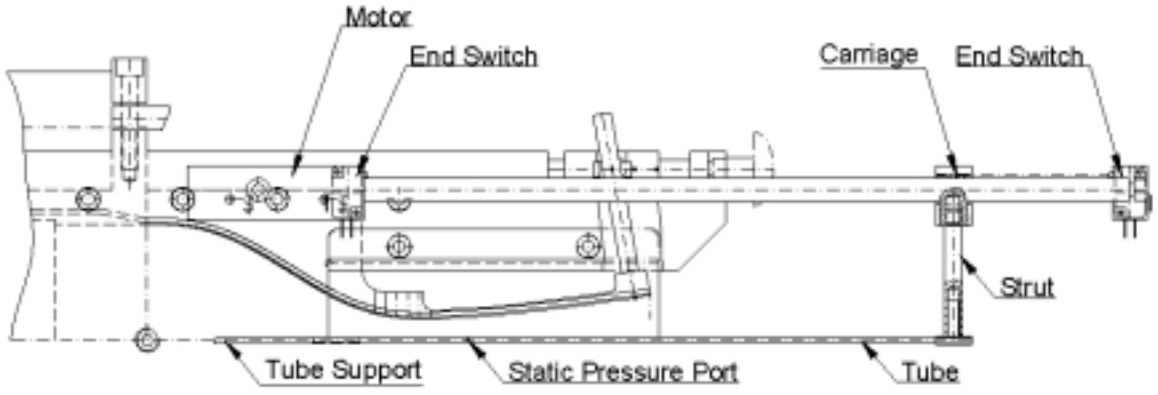

Fig.4 Schematic of centerline static pressure measurement system.

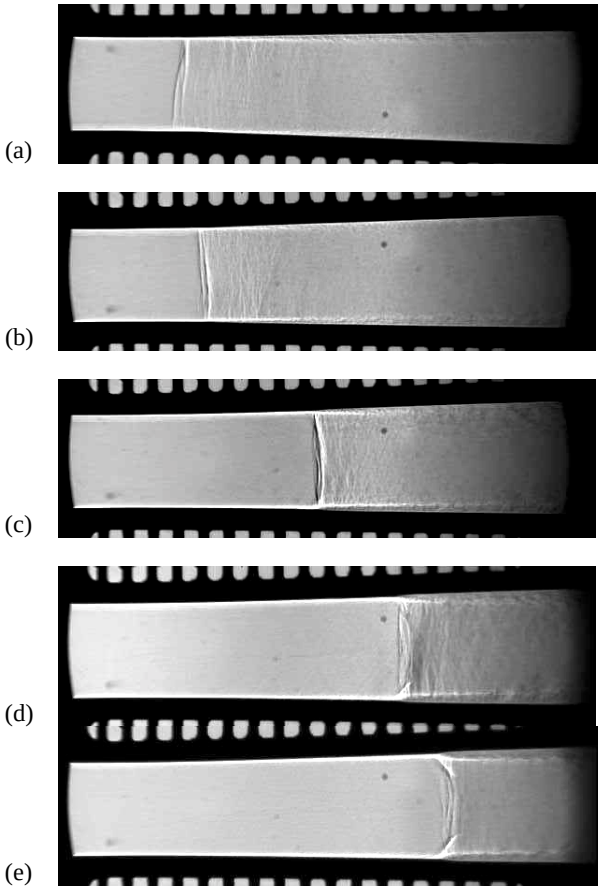

Fig.5 Schlieren images of shock with increasing nozzle pressure ratio for $A_e/A_t = 1.20$. NPR=(a) 1.28; (b) 1.28; (c) 1.35; (d) 1.40; (e) 1.55.

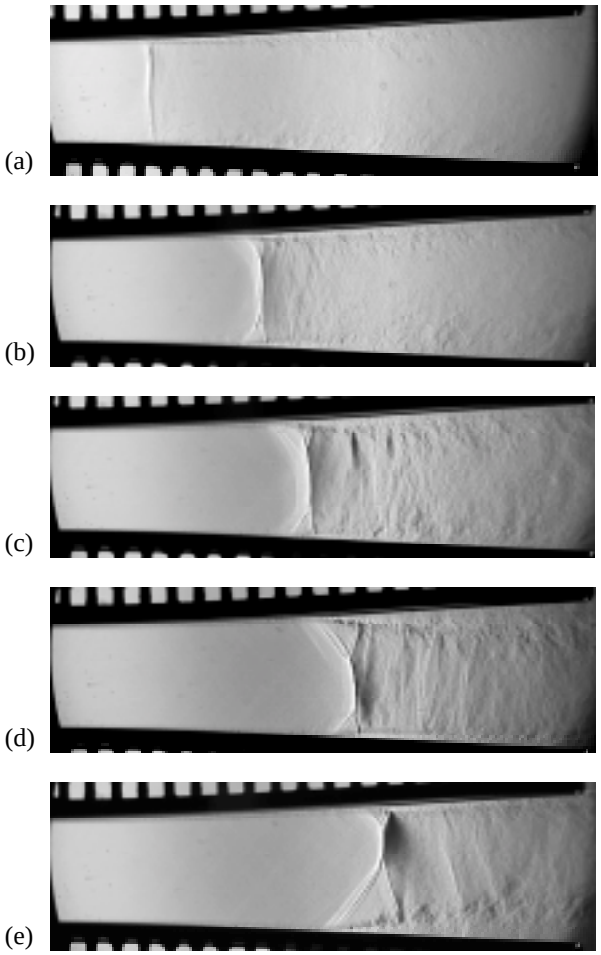

Fig.6 Schlieren images of shock with increasing nozzle pressure ratio for $A_e/A_t = 1.40$. NPR=(a) 1.20; (b) 1.33; (c) 1.44; (d) 1.59; (e) 1.77.

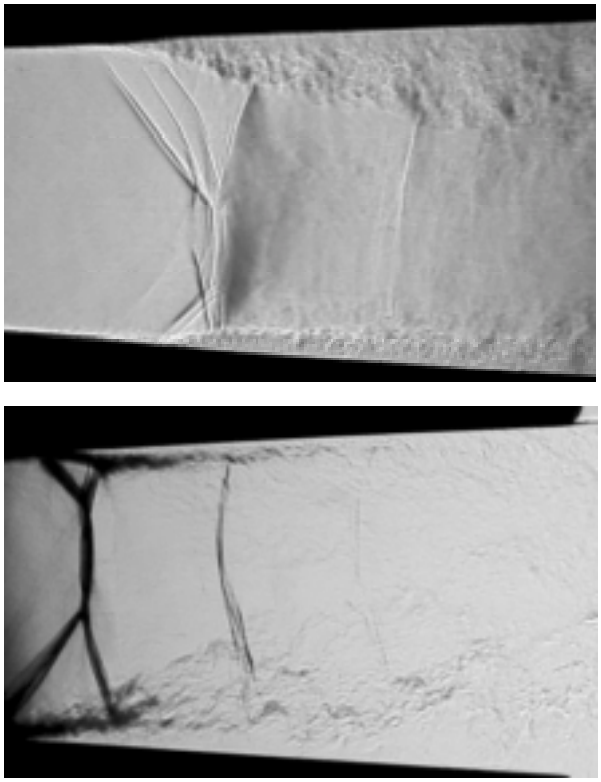

Fig.7 Details of shock and separated flow for $A_e/A_t = 1.5$ and NPR=1.5. The two pictures were taken with slightly different illumination settings and fields of view.

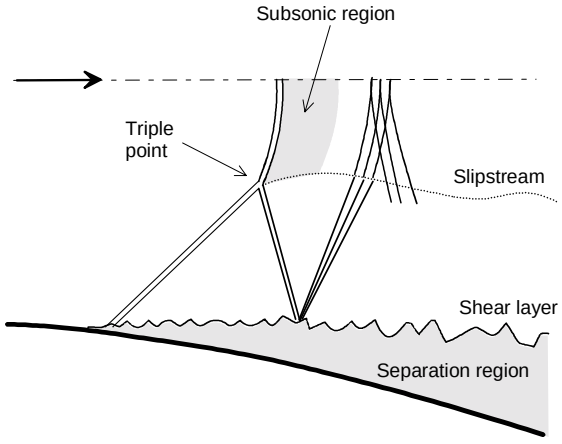

Fig.8 Conjecture on shock and fluid phenomena.

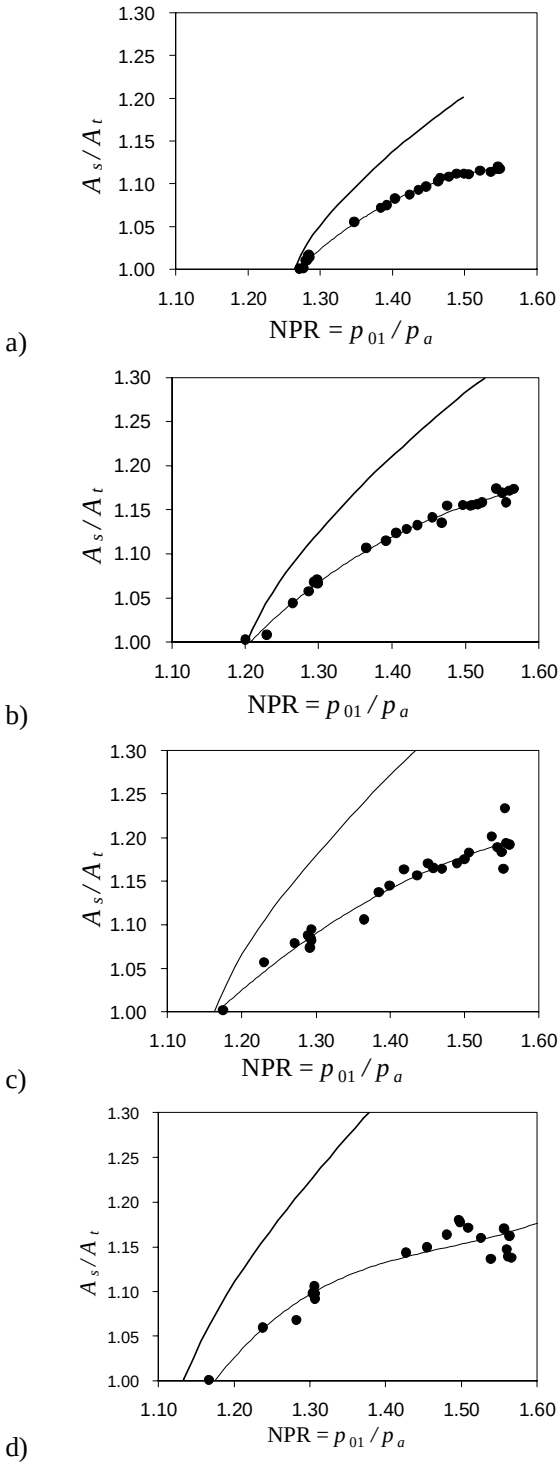

Fig.9 Shock Location versus NPR for A_e/A_t = (a) 1.20; (b) 1.30; (c) 1.40; (d) 1.50. Thin line is best fit of data, thick line is prediction of one-dimensional inviscid theory.

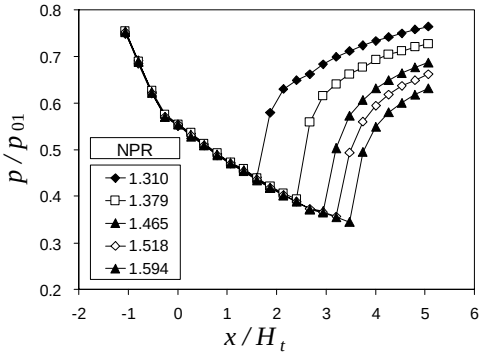

a)

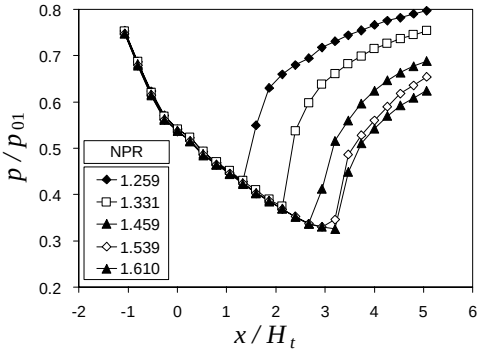

b)

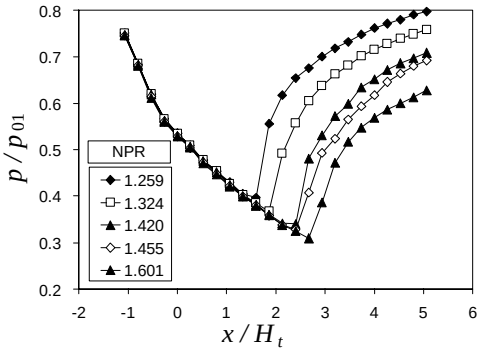

c)

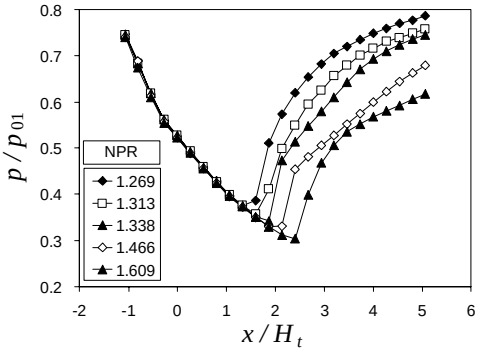

d)

Fig.10 Static pressure distribution on the upper wall of a nozzle A_e/A_t = = (a) 1.20; (b) 1.30; (c) 1.40; (d) 1.50.

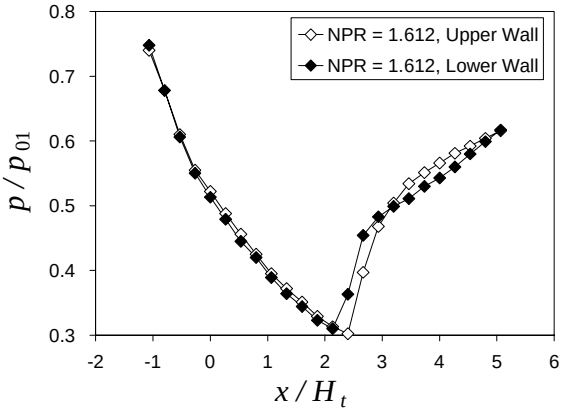

Fig.11 Static pressure distributions on the upper and lower walls of the nozzle.

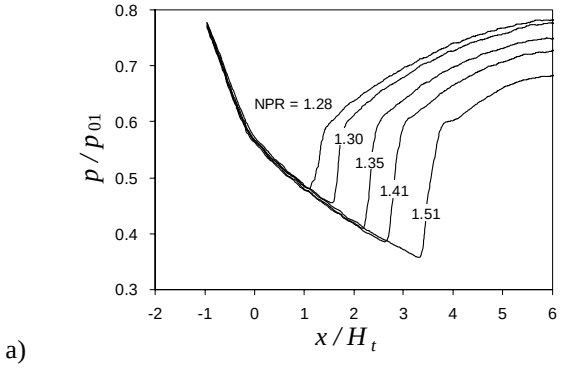

a)

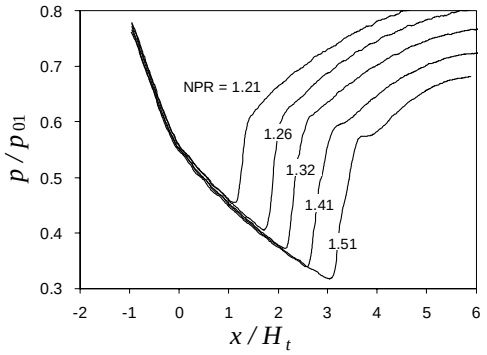

b)

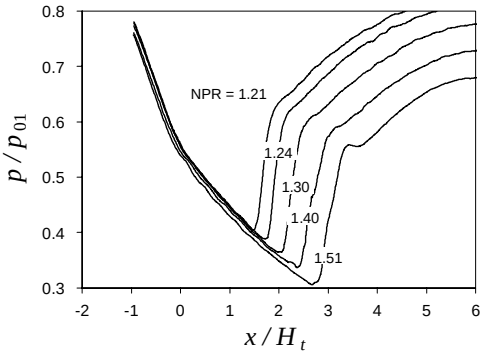

c)

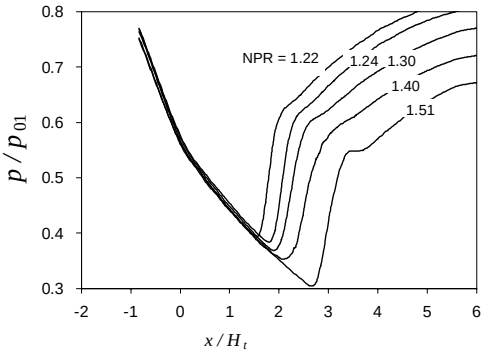

d)

Fig.12 Centerline pressure distribution versus NPR for A_e/A_t = = (a) 1.20; (b) 1.30; (c) 1.40; (d) 1.50.

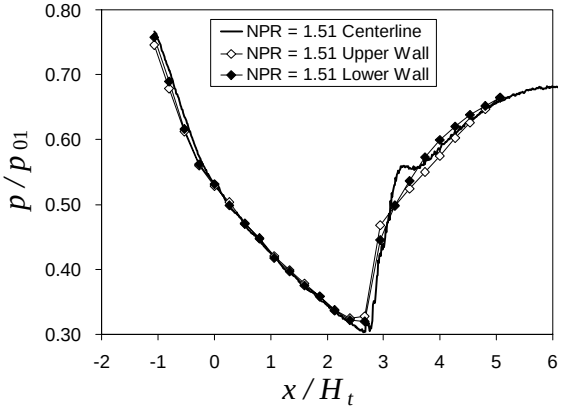

Fig.13 Comparison of wall versus centerline pressure distribution for $A_e/A_t = 1.4$.

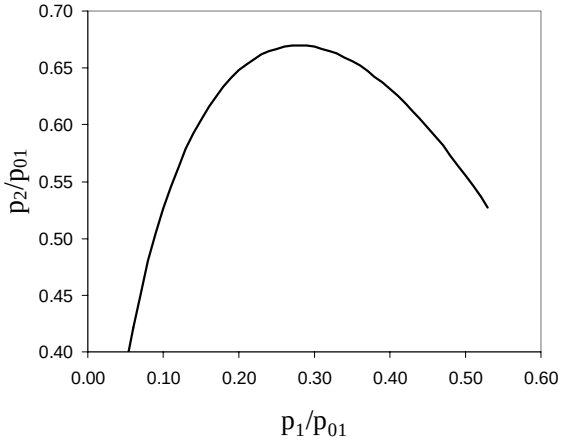

Fig.14 Normal shock relation for the static pressures before and after the shock.

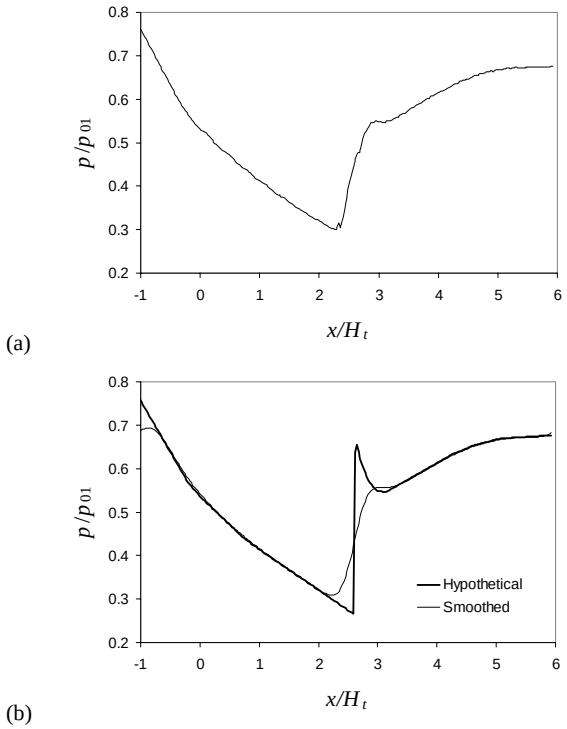

Fig.15 Centerline pressure distribution for $A_e/A_t = 1.4$ and NPR=1.5. (a) Actual; (b) hypothetical without and with Gaussian smoothing.

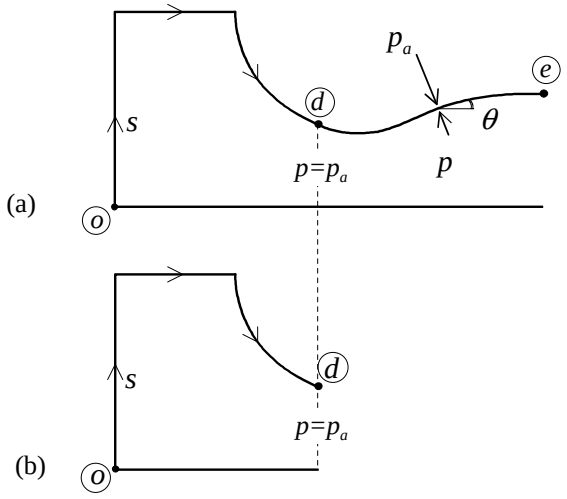

Fig.16 Procedure for calculating thrust of (a) actual nozzle and (b) ideal nozzle.

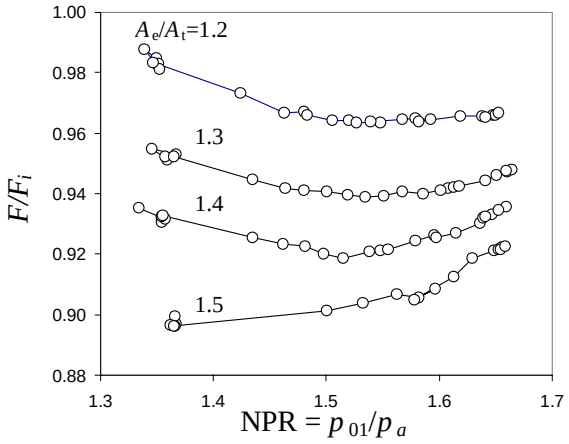

Fig.17 Thrust coefficient versus NPR for various area ratios.

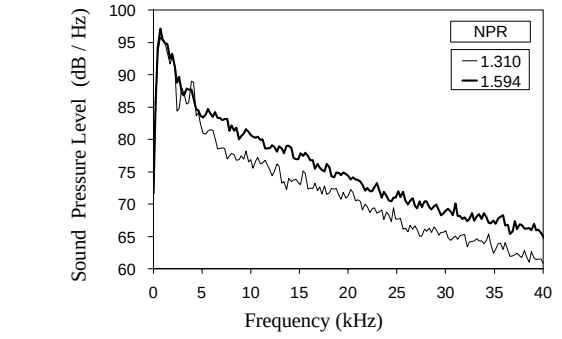

a)

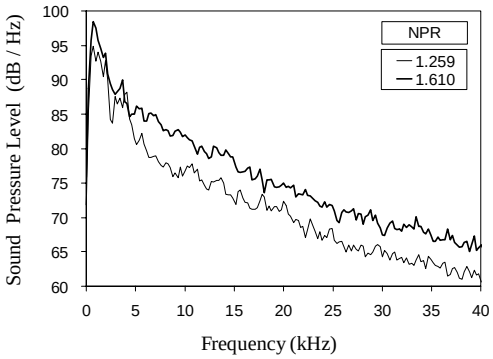

b)

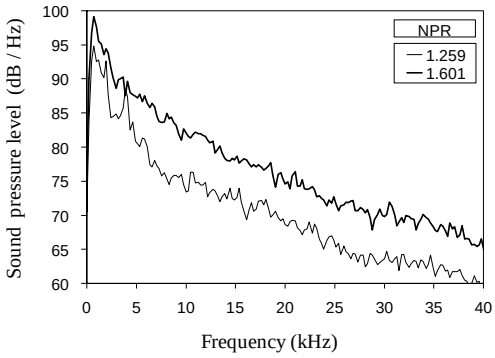

c)

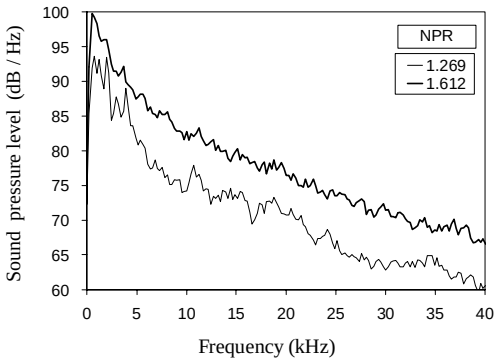

d)

Fig.18 Noise spectra for A_e/A_t =(a) 1.20; (b) 1.30; (c) 1.40; (d) 1.50.

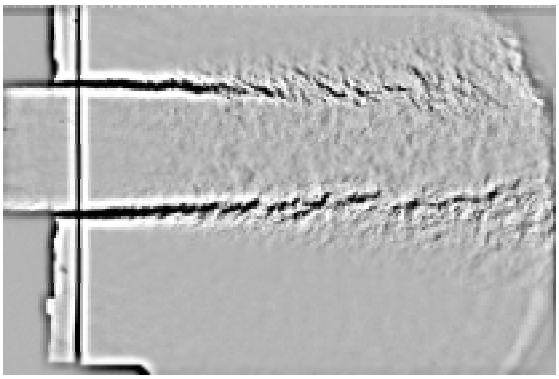

(a)

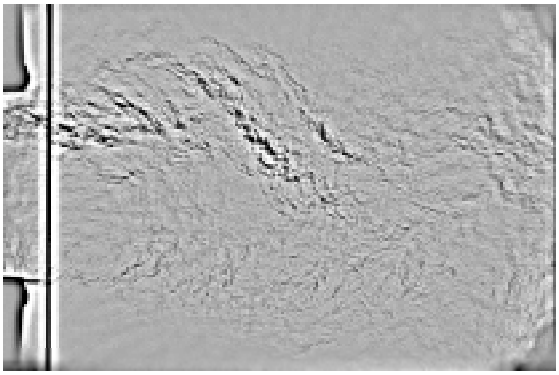

(b)

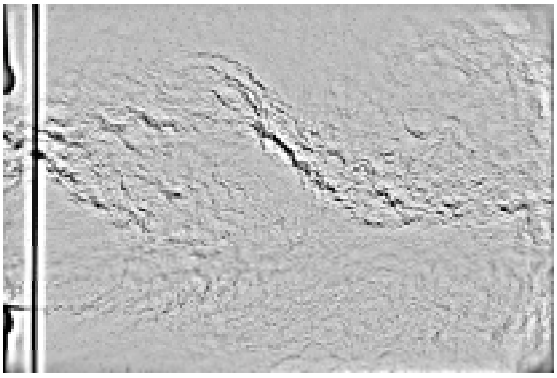

(c)

Fig.19 Enhanced spark schlieren images of the external flow at NPR around 1.5 and for A_e/A_t= (a) 1.0; (b) 1.4; (c) 1.5.